Chemical Science

ROYAL SOCIETY OF CHEMISTRY

EDGE ARTICLE

View Article Online
View Journal | View Issue

Cite this: *Chem. Sci.*, 2025, **16**, 15638

All publication charges for this article have been paid for by the Royal Society of Chemistry

Photothermal therapy for bacteria-infected wound healing *via* a cation–anion inverted antiperovskite with full-spectrum solar absorption†

Xuejiao Wang,‡[a] Lianbo He,‡[a] Qiyang Cai,[a] Zhi Su,[a] Zhengjun Huang,[a] Hao Sun,[a] Yuhui Lai,[c] Zheyan Chen,[c] Jianbin Ye,[b] Yan Yu,[c] Zhigang Zou,[d] Hanlin Huang *[c] and Hu Zhu *[ab]

Clinical treatment of open wounds is challenging due to bacterial infection and biofilm protection. Antibiotics are commonly utilized as antibacterials; however, multidrug resistance (MDR) severely affects the therapeutic effect. Therefore, developing a non-antibiotic strategy for treating infections and accelerating wound healing is highly required. Herein, for the first time, an electronically inverted antiperovskite, $InNNi_3$, has been demonstrated as a novel photothermal material with efficient and broad-spectrum anti-bacterial activity. Due to the quasi-continuous energy levels and inverse coordination with cations/anions exchanged in crystal sites, $InNNi_3$ possesses a near-unity photothermal conversion efficiency (96.9%) and a positively charged surface, which together contribute to the high antimicrobial activity (99.9%) *via* photothermal activation and electrostatic interaction with pathogens, including *methicillin-resistant Staphylococcus aureus* (*MRSA*), *Escherichia coli* (*E. coli*) and *Candida albicans* (*C. albicans*) within several minutes. Moreover, as an effective antibiofilm agent, $InNNi_3$ exhibits over 99% scavenging effect on biofilms. An accelerated healing rate for infected wounds has also been achieved using an $InNNi_3$-treatment strategy under NIR irradiation by reducing inflammation, promoting collagen deposition, boosting early expression of CD31 and facilitating the regeneration of dermis and skin appendages. The excellent biocompatibility of $InNNi_3$ further demonstrates its great potential for clinical applications in future.

Received 13th May 2025
Accepted 22nd July 2025

DOI: 10.1039/d5sc03456f

rsc.li/chemical-science

Introduction

Skin, as the largest organ of the human body and primary defensive barrier, plays a pivotal role in protecting the organism from pathogenic invasions and preventing infections.[1,2] Given its exposure to the external environment, the skin is inherently vulnerable to injury and wound formation. Wound healing is a physiological complex process with different stages, including the clearance of foreign bodies, inflammatory response, formation of granulation tissue, and maturation of scar tissue.[1,3,4] However, bacterial infections often become a major obstacle to wound healing, which not only exacerbates the inflammatory response leading to prolonged healing time but also induces some serious complications such as intense pain, amputation, and even death.[5–7] In clinical practice, antibiotics are widely used for the treatment of bacterial infections,[8] while the overuse of antibiotics has led to the emergence of multi-drug-resistant (MDR) bacterial pathogens such as *methicillin-resistant Staphylococcus aureus* (*MRSA*), which demonstrates a high level of resistance to most conventional antibiotics.[9–12] More seriously, the development pace of new antibiotics with stronger activity against drug-resistant bacteria is still far from sufficient to effectively counter the evolution and variation of bacterial resistance.[13–15] Therefore, developing novel antibacterial strategies based on new mechanisms that are different from traditional antibiotics for anti-infection treatment is highly required.

Photothermal therapy (PTT), as a promising non-invasive anti-infective method, has attracted widespread attention due to its safety, remote controllability, precision treatment and broad-spectrum antibacterial properties.[16,17] The photothermal

[a]*Fujian-Taiwan Science and Technology Cooperation Base of Biomedical Materials and Tissue Engineering, Engineering Research Center of Industrial Biocatalysis, Fujian Provincial Key Laboratory of Advanced Materials Oriented Chemical Engineering, College of Chemistry and Materials Science, Fujian Normal University, Fuzhou, Fujian 350007, China. E-mail: zhuhu@fjnu.edu.cn*

[b]*Key Laboratory of Translational Tumor Medicine in Fujian Province, Putian University, Putian 351100, China*

[c]*Key Laboratory of Eco-materials Advanced Technology, College of Materials Science and Engineering, Fuzhou University, Fuzhou 350108, China. E-mail: huanghanlin@fzu.edu.cn*

[d]*Eco-materials and Renewable Energy Research Center (ERERC), National Laboratory of Solid State Microstructures and Department of Physics, Nanjing University, Nanjing 210093, China*

† Electronic supplementary information (ESI) available. See DOI: https://doi.org/10.1039/d5sc03456f

‡ These authors contributed equally to this work and are joint first authors.

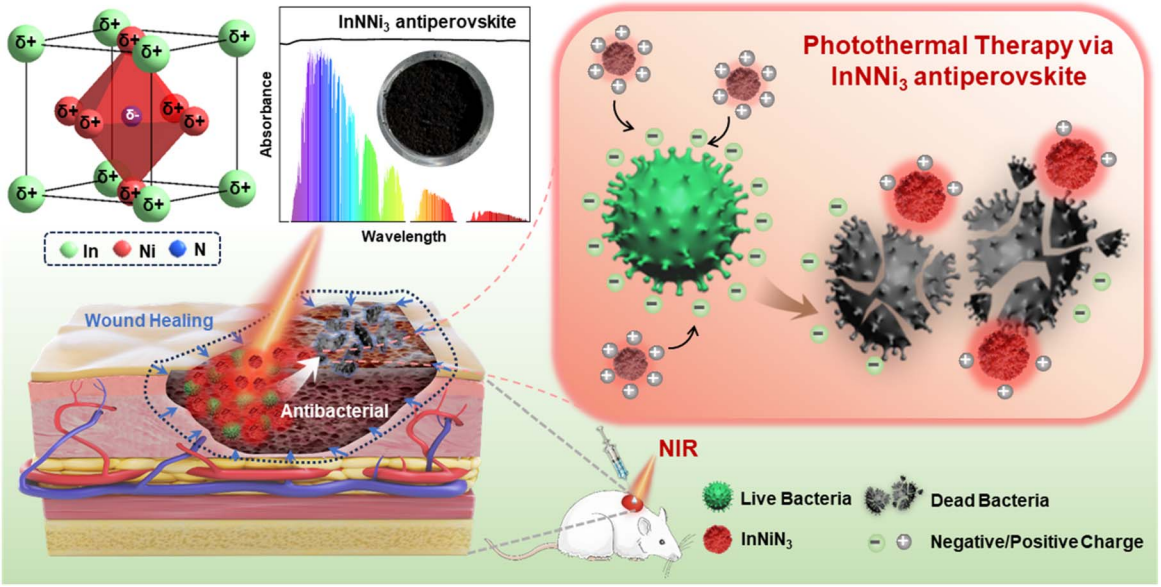

Scheme 1 Schematic illustration of the photothermal antibacterial process utilizing the antiperovskite-type photothermal material $InNNi_3$ with strong, full-spectrum solar light absorption and through electrostatic interaction between negative bacteria and positive $InNNi_3$.

antibacterial mechanism is based on the conversion of photon energy into heat by a photothermal agent (PTA), causing localized hyperthermia that denatures proteins, damages DNA, disrupts the bacterial structure, and inhibits key enzymes, thereby inactivating or decomposing bacteria.[18,19] Commonly used photothermal materials include noble metals,[20,21] oxide/sulfide semiconductors,[22] two-dimensional metal carbides/nitrides,[23] metal–organic frameworks (MOFs)[24] and covalent organic frameworks (COFs).[25,26] Although progress has been made for developing various photothermal materials, lots of challenges and problems are still required to be addressed. The high cost of noble metals limits their practical clinical applications.[27,28] Oxide/sulfide semiconductors always have large bandgap values,[29] which result in a narrow range of light absorption, and these compounds are usually unstable in an acidic physiological environment. The synthetic processes of two-dimensional metal carbides/nitrides, such as MXenes, are relatively complicated with a low yield of final product, making it very difficult for batch preparation.[30] Carbon-based organic materials face limitations, including thermal instability at elevated temperatures,[24,31] difficulty in dispersion and potential adverse effects on biological systems such as impaired gastrointestinal motility. Therefore, the development of novel photothermal materials with high absorption coefficients, broad spectral light capturing, near-unity photothermal conversion efficiency, excellent photo/thermal stability, good biocompatibility and low biotoxicity, as well as the ability to be prepared in large quantities, are highly significant to photothermal clinical applications. Based on the above considerations, an emerging and novel type of material family, ANX_3-type antiperovskite nitrides, with great potential for photothermal conversion applications, which remains to be developed, has garnered our significant attention and interest.

For the ANX_3 chemical formula, A/X sites represent metal elements (the A site always includes In/Zn/Cu metals and the X site usually consists of Ni/Co/Fe, group VIII transition metals) and the N site is the nitrogen element.[32] ANM_3 can be regarded as an electronically inverted perovskite derivative with cations/anions exchanged in crystallographic sites of coordinated polyhedra with N anions located in the center and six X-site metal cations at corners,[33] $[N^{\delta-}X_6^{\delta+}]$, which is totally inversed compared with the commonly shown coordination in traditional perovskites,[34] such as $Pb^{\delta+}I_6^{\delta-}$. Thus, unusual bonding modes for X-site metal cations are presented, such as X–X metal bonds, linear X–X–X linkages and the X-rich surface with abundant exposed metal sites, which also show similar characteristics to intermetallic compounds with N elements in the metal lattice.[35] Compared with other photothermal materials, inverse coordinative structures endow ANX_3 antiperovskites with two important properties for photothermal antibacterial: (1) a similar electronic structure to conductors with quasi-continuous energy levels which exhibits full-spectrum solar light capturing and high absorption ability,[36] leading to excellent light-to-heat conversion efficiency; (2) an electronically inverted coordination of anions/cations contributing to the positively charged surface which enhances the affinity with the negatively charged outer membrane of pathogens through electrostatic interactions.[37] Besides, the chemical component of ANX_3 antiperovskite is flexibly adjustable,[38] which is beneficial for the regulation of biocompatibility and cytotoxicity that are important for the safety of applicable biomedical materials. To the best of our knowledge, the use of antiperovskite nitrides as photothermal materials has never been reported.

Herein, for the first time, a unique class of photothermal material, $InNNi_3$ antiperovskite nitride (Scheme 1), has been

developed for antibacterial treatment and wound healing under NIR irradiation. $InNNi_3$, as a novel light absorber, possesses an absorption area across the whole solar spectrum due to its quasi-continuous energy levels, exhibiting a near-unity solar-thermal conversion efficiency of 96.91%. Electronically inverted coordination of anions/cations in the crystal structure endows $InNNi_3$ with a positively charged surface with an obviously positive zeta potential value contributed by the exposed $In^{\delta+}$/$Ni^{\delta+}$ metallic sites with mixed valences, which induce strong electrostatic interactions with negatively charged pathogens. $InNNi_3$ with a synergistic antimicrobial effect successfully realizes an efficient photothermal elimination ratio (99.9%) of various typical microbes, including *methicillin-resistant Staphylococcus aureus* (*MRSA*), *Escherichia coli* (*E. coli*) and *Candida albicans* (*C. albicans*). Besides, $InNNi_3$ also shows a satisfactory scavenging effect on biofilms of different bacteria. An accelerated rate of skin wound healing with the assistance of $InNNi_3$ under light irradiation is achieved as well. Moreover, the excellent biocompatibility of $InNNi_3$ exhibits great potential as a practical photothermal agent for clinical applications. Therefore, the NIR-triggered $InNNi_3$ provides a safe and highly efficient alternative candidate for the development of a light-assisted therapeutic platform for severe bacterial infections and wound healing.

Results and discussion

Structural and surface characterization studies of $InNNi_3$ antiperovskite

The synthesis of $InNNi_3$ was carried out according to a nitridation method from a hydroxide precursor. Scanning electron microscopy (SEM) reveals that the $InNNi_3$ nanoparticles exhibit a coral reef-like aggregate morphology with uniform nanoscale dimensions (Fig. 1a). Transmission electron microscopy (TEM) (Fig. 1b) confirms the homogeneous morphology of the as-synthesized $InNNi_3$ nanoparticles. Moreover, the high-resolution transmission electron microscopy (HRTEM) image of a typical $InNNi_3$ nanoparticle (Fig. 1c) exhibits clear lattice fringes with a crystal spacing of 0.274 ± 0.002 nm corresponding to the (110) facet of $InNNi_3$. The inset of Fig. 1c shows the fast Fourier transform (FFT) of the HRTEM area, which shows the corresponding diffraction spots of several facets. Simulation of the crystal structure of $InNNi_3$ is shown as a three-dimensional atomic model consistent with a crystal plane arrangement (Fig. 1d), which exhibits a clearer view of the surface structure at the atom-scale level. The characterization results of high-angle annular dark-field scanning transmission electron microscopy (HAADF-STEM) as well as energy dispersive X-ray spectroscopy (EDS) are shown in

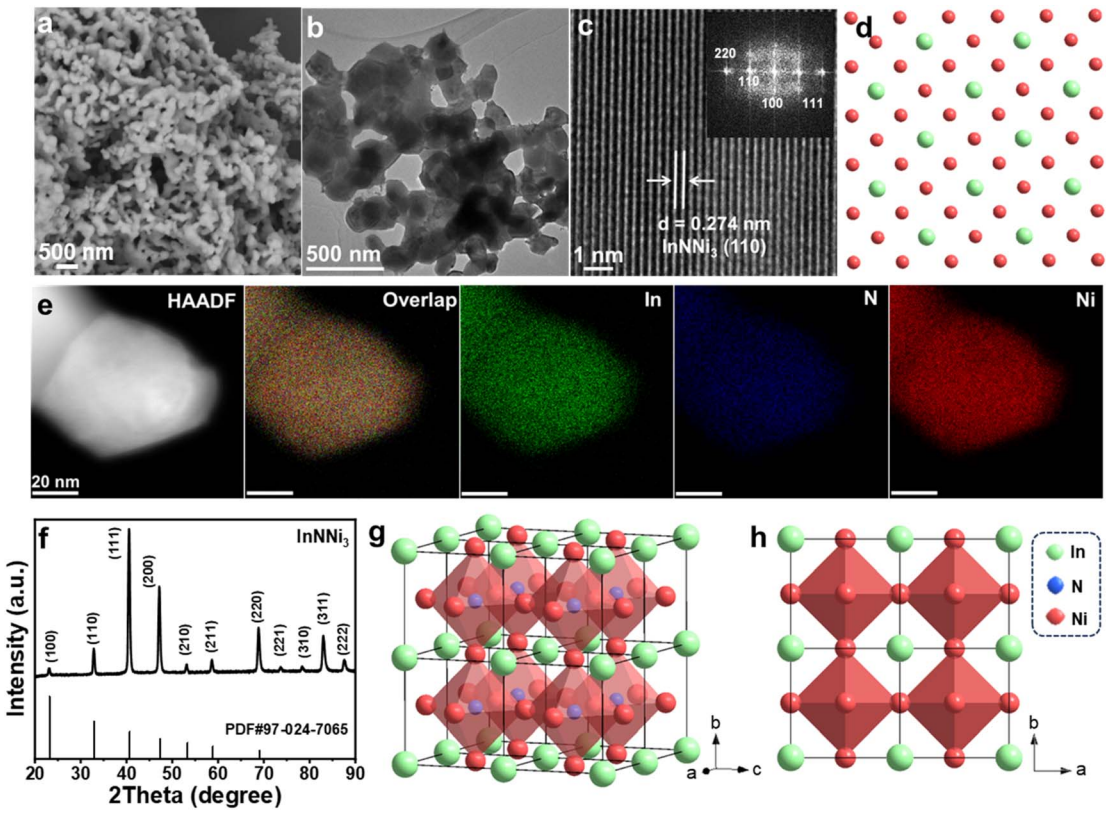

Fig. 1 Morphology, surface and crystal structure characterization of $InNNi_3$. (a) SEM image. (b) TEM image. (c) HRTEM image (inset shows the FFT of the corresponding HRTEM area). (d) Simulated atomic models viewed from the same direction as images in panel (c) (In: cyan; Ni: red). (e) HAADF-STEM and EDS mapping images of In/N/Ni elements. (f) Powder XRD patterns. (g and h) Crystal structure viewed from different directions.

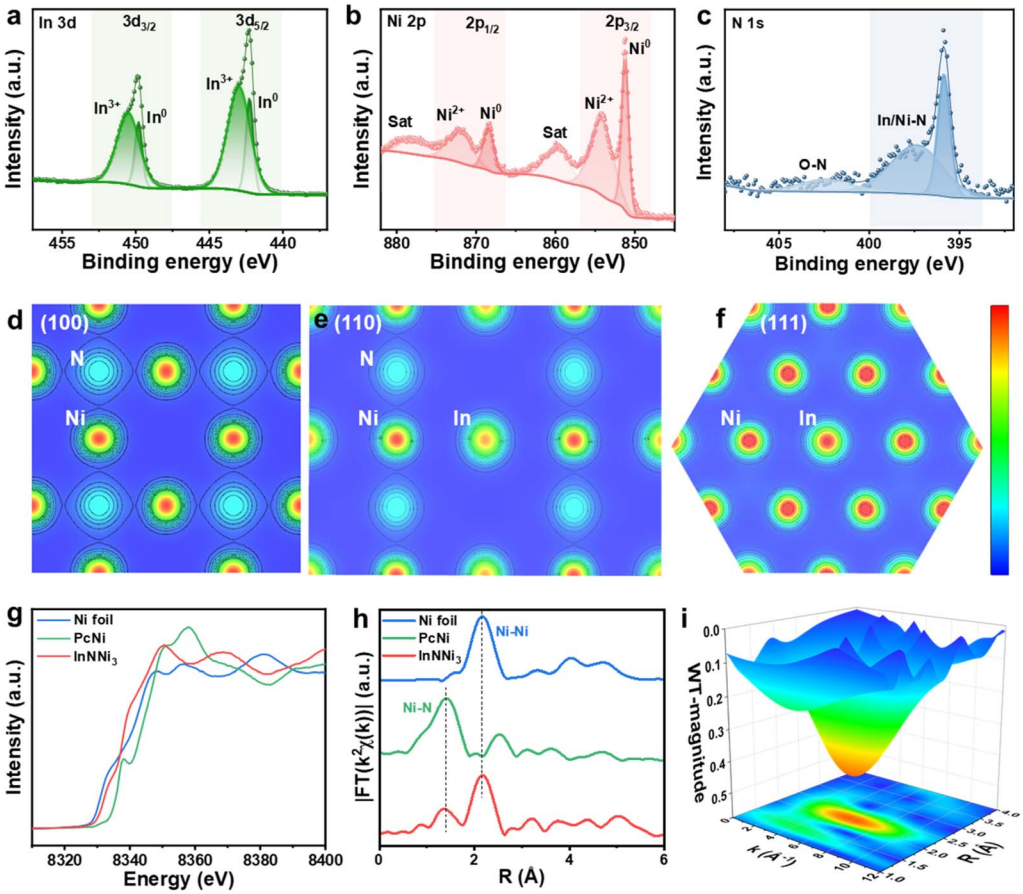

Fig. 2 Surface chemical state, charge density distribution and local coordination of $InNNi_3$ antiperovskite. XPS spectra: (a) In 3d, (b) Ni 2p and (c) N 1s. Charge density isosurface at different crystal facets: (d) (100), (e) (110), and (f) (111). (g) Ni K-edge XANES spectra. (h) Magnitude of Fourier transformed Ni K-edge EXAFS data. (i) WT-EXAFS signal at the Ni K-edge.

Fig. 1e. The elements of In, N, and Ni are highly dispersed in $InNNi_3$ nanoparticles, and the elemental ratio of In : N : Ni is measured as 2.174 : 2.118 : 5.708, which is close to the stoichiometric ratio of $InNNi_3$ (Fig. S1†). Fig. 1f shows the powder X-ray diffraction (PXRD) pattern of the as-prepared $InNNi_3$ particles. All diffraction peaks of $InNNi_3$ are in good agreement with its standard reference (PDF#97-024-7065), showing high phase purity and good crystallinity. Fig. 1g and h show the crystal structure of the $InNNi_3$ antiperovskite nitride, which has a cubic lattice similar to that of a conventional perovskite oxide ($CaTiO_3$) or halide ($CsPbBr_3$). $InNNi_3$ is an ANM_3-type perovskite-structured nitride with exchanging crystal sites of cations and anions (antiperovskite), and its crystal structure belongs to the cubic crystallographic system. $InNNi_3$ has an unusual and electronically inverted coordination octahedron, $[NNi_6]$, with the Ni cations (with partially positive charge) located at the corner of the $[NNi_6]$ octahedron, while the nitrogen (N) anion (with partially negative charge) is located at the center. This coordination chemistry is completely different from that of traditional perovskites, with a cation in the center and anions as ligands at the corners. Therefore, $InNNi_3$ is a unique antiperovskite material with inverted electronic characteristics. Indium (In) cations (also partially positively charged) fill the spaces between the $[NNi_6]$ octahedra, which serve to stabilize the crystal structure and balance charges. The surface of $InNNi_3$ is positively charged due to the exposure of numerous positively charged Ni/In metallic sites, which is further proved by surface chemical states of In/Ni and the measured results of zeta potential of $InNNi_3$ nanoparticles in the following text, facilitating their electrostatic interaction with negatively charged bacteria.

X-ray photoelectron spectroscopy (XPS) analysis was performed to investigate the surface electronic properties and chemical valence states of $InNNi_3$, as shown in Fig. 2a–c (C 1s and survey spectra are shown in Fig. S2†). XPS results show that the valence states of In and Ni elements on the surface of $InNNi_3$ possess mixed valence states as In^0/In^{3+} and Ni^0/Ni^{2+}, respectively, which also indicate that metal sites on the surface of $InNNi_3$ have a partially positive charge. The calculated charge density isosurface results of (100), (110) and (111) facets are shown in Fig. 2d–f and S3,† which obviously demonstrate that the charges are mainly accumulated at Ni sites and partially distributed in sites, while N sites show a relatively low charge density. Combined with XPS results, the high charge density located at Ni/In sites with a partially positive charge would contribute to the positively charged surface of $InNNi_3$. X-ray absorption spectroscopy (XAS) was utilized to investigate the valence state and the local coordination of Ni element in the

bulk $InNNi_3$ material. PcNi (nickel phthalocyanine) and standard Ni metal foil were also characterized for comparison. X-ray absorption near-edge structure (XANES) spectra are shown in Fig. 2g; the onset peak of $InNNi_3$ is located at a position between that of Ni and PcNi, showing a positive or negative position compared to that of Ni or PcNi, respectively. Thus, the valence of Ni in $InNNi_3$ antiperovskite is a positive value between 0 and +2, demonstrating a mixed valence state with a partially positive charge, which is consistent with the XPS result of Ni 2p. According to the E_0 positions, a chemical state of Ni element in $InNNi_3$ can be calculated as +0.4 (Fig. S4†).[39] Besides, the pre-edge peak at 8338 eV observed in PcNi is not found in the XANES curve of $InNNi_3$, which is regarded as the characteristic signal of the Ni–N_4 structure,[40] thus suggesting a different coordination structure of Ni in $InNNi_3$. This phenomenon can be explained by unique coordination chemistry in the crystal structure of $InNNi_3$ antiperovskite, in which each Ni is coordinated to 2 adjacent N atoms. As for the Ni K-edge of extended X-ray absorption fine structure (EXAFS) spectra (Fig. 2h), two main peaks at 1.37 Å and 2.17 Å, can be assigned to Ni–N coordination in the first shell and a Ni–Ni metallic bond in the second shell. As shown in Fig. 2i, the wavelet transform (WT) of Ni K-edge EXAFS further clearly shows the different local coordination environment with Ni–N and Ni–Ni in $InNNi_3$. Based on the XPS and XAS results, $InNNi_3$ antiperovskite exhibits a positively charged state on the surface as well as an analogous chemical component and a coordination structure similar to metals or intermetallic compounds, causing efficient electrostatic interaction with negatively charged bacteria and a continuous energy level distribution related to its full-spectrum solar absorption, which is beneficial for the photothermal antibacterial application.

Electronic and photothermal properties of $InNNi_3$ antiperovskite

In order to deeply investigate the energy band structure and electronic properties of the $InNNi_3$ antiperovskite material and understand its photophysical properties, a density functional theory (DFT) calculation method was utilized to analyze the distribution of energy levels (Fig. 3a) and the density of states (DOS, Fig. 3b). The calculation results reveal that $InNNi_3$ antiperovskite nitride has a quasi-continuous arrangement of energy levels and density of states near the Fermi energy level, exhibiting conductor properties with a near-zero bandgap, which absorbs photon energy across the entire solar spectrum

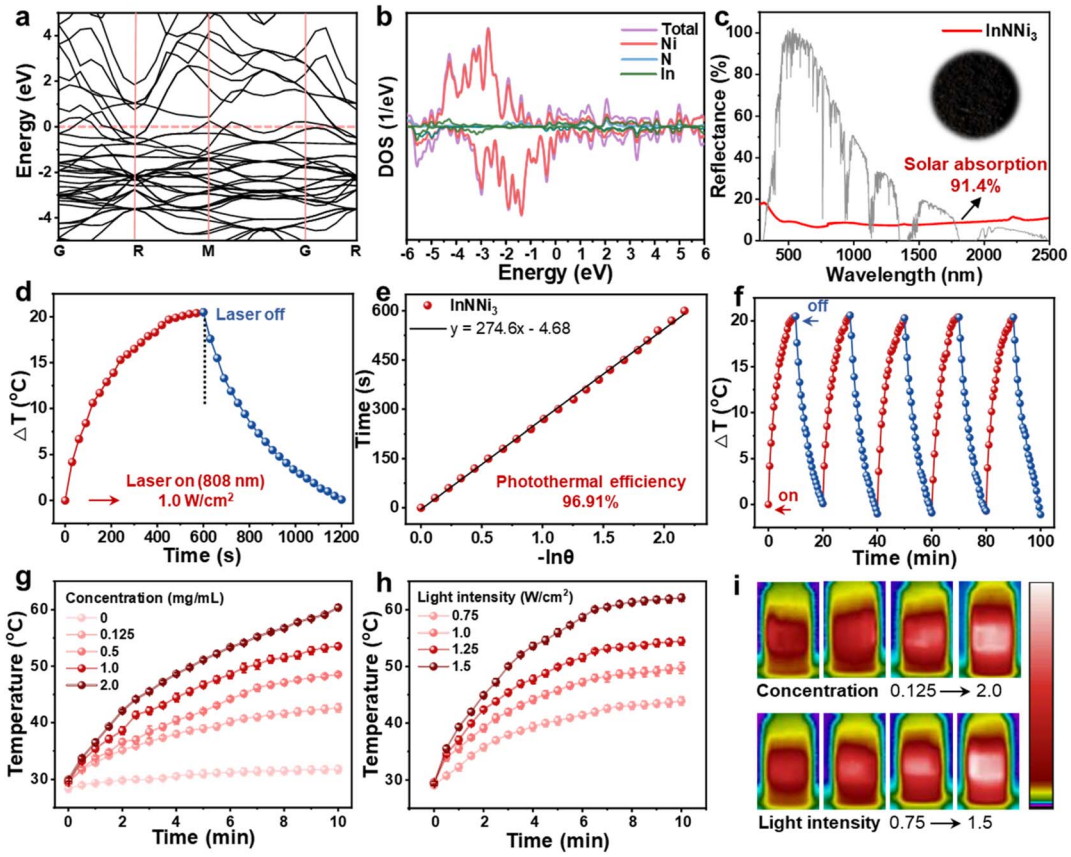

Fig. 3 Photophysical and photothermal properties of $InNNi_3$. (a) Calculated energy band structure. (b) Calculated density of states (DOS) for Ni, N, and In elements. (c) Diffuse reflectance spectra (DRS) of powders. (d) A typical time-dependent temperature variation curve under solar light irradiation and after the irradiation is turned off. (e) Natural cooling and a plot fitting of cooling time *versus* − ln(*θ*). (f) Temperature profiles during on/off cycles with or without light irradiation. Temperature profiles of $InNNi_3$ dispersed in water under 808 nm laser irradiation with different concentrations (g) and light intensities (h). (i) Corresponding infrared imaging photographs of panels (g) and (h).

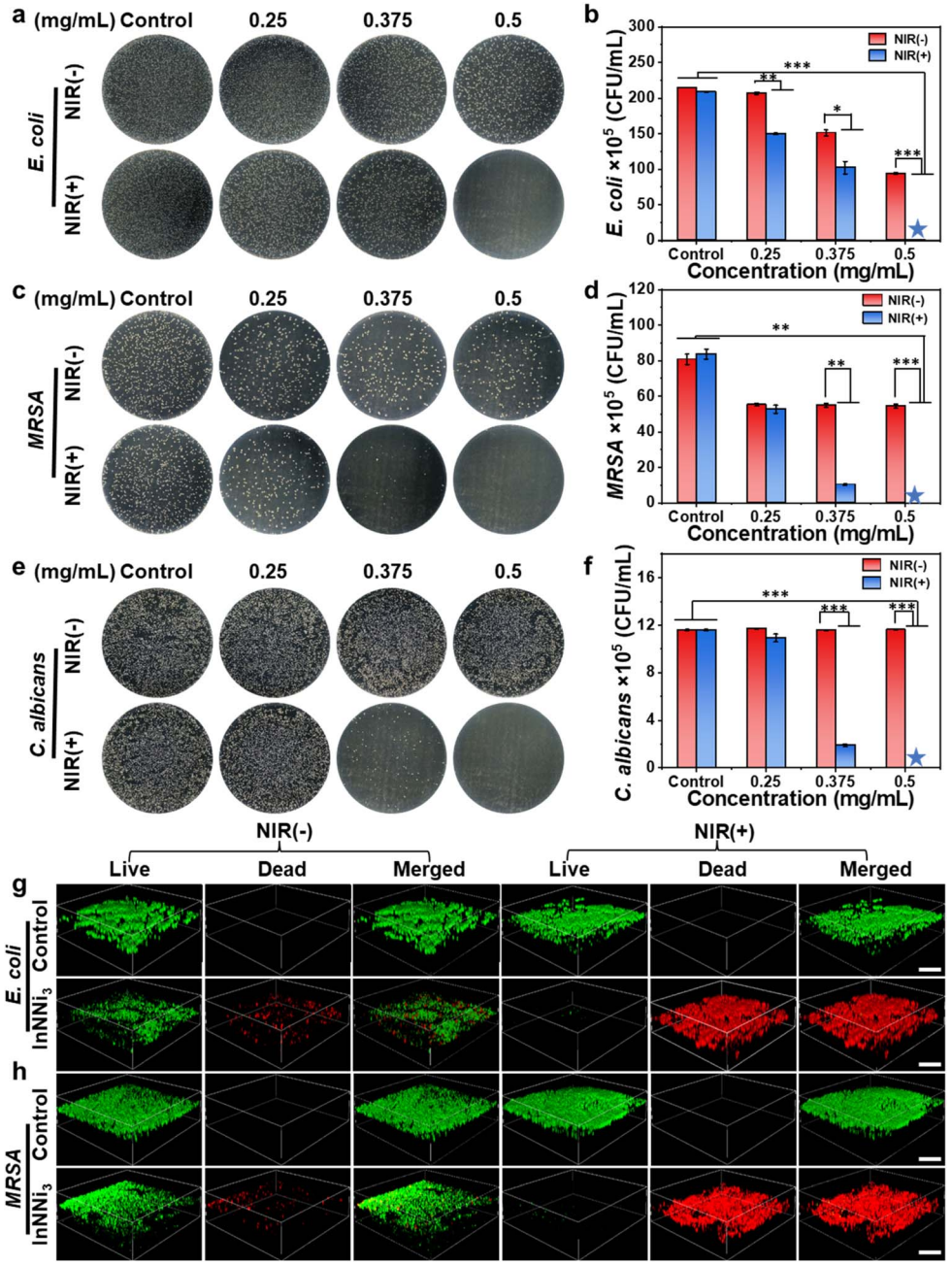

Fig. 4 Evaluation of *in vitro* antimicrobial and antibiofilm performances of $InNNi_3$. (a–f) Photographs and quantitative results of microbial colonies treated with different concentrations of $InNNi_3$ with (NIR(+)) or without (NIR(−)) 808 nm NIR laser (1.0 W cm^{-2}) irradiation for 10 min. Pentagrams in the graph represent less than 1%. (g and h) Live/dead staining of *E. coli* and *MRSA* formed biofilms after different treatments. Scale bar, 30 μm. Data are expressed as mean ± standard deviation, $n = 3$. * indicates statistically significant differences (*$p < 0.05$, **$p < 0.01$, and ***$p < 0.001$).

(Fig. 3c) with 91.4% (ultraviolet: 6.0%, visible: 45.9%, and near infrared: 39.5%) solar absorption, showing a dark black color. The photothermal conversion efficiency of $InNNi_3$ was quantitatively measured according to the cooling curve after a period of time with 808 nm laser irradiation, and the conversion efficiency of $InNNi_3$ was calculated to be as high as 96.9% (Fig. 3d and e). The calculation methods are shown in the ESI.† Besides, the experimental setup for the measurement of photothermal conversion efficiency and the corresponding infrared imaging photographs are shown in Fig. S5.† The results demonstrate that the $InNNi_3$ antiperovskite with full-spectrum absorption has a very strong solar-to-thermal conversion. As shown in Fig. S6,† the high thermal stability of $InNNi_3$ is also demonstrated by thermogravimetric analysis (TGA), without any weight loss over 400 °C, showing great potential as a stable photothermal material for practical applications. $InNNi_3$ has excellent cyclic photothermal conversion stability during repetitive on/off irradiation experiments (Fig. 3f). The

photothermal conversion performance of $InNNi_3$ dispersed in water (similar to the photothermal bacterial environment) was further investigated. The effects of concentration of $InNNi_3$ and light intensity of 808 nm laser on temperature increase *via* photothermal conversion are shown in Fig. 3g and h. Under irradiation of 1 W cm^{-2}, with the concentration increasing from 0 to 2.0 mg mL^{-1}, the temperature variation value increases from 13.1 °C to 30.4 °C (Fig. 3g). Meanwhile, at the same concentration of 0.5 mg mL^{-1}, the temperature gradually improves from 14.8 °C to 32.7 °C after 10 min of irradiation at a light density of 1.0 W cm^{-2}. Fig. 3i shows the corresponding infrared imaging photographs of experimental results in Fig. 3g and h. These results indicate that the higher concentration and light intensity both enhance the photothermal conversion effect.

In Vitro antimicrobial and antibiofilm properties of $InNNi_3$

Given its exceptional photothermal conversion properties and positively charged surface, the plate counting method was employed to quantitatively measure its activity against a range of bacterial and fungal strains, including the Gram-negative bacterium *E. coli*, the Gram-positive bacterium *MRSA*, and the fungus *C. albicans*. As shown in Fig. 4a–f, a pronounced inhibitory effect of $InNNi_3$ on the proliferation of *E. coli*, *MRSA*, and *C. albicans* is observed following exposure to an 808 nm NIR laser, outperforming that of experimental groups without light irradiation and the control group. The inhibition rate increases with the increase of concentration of $InNNi_3$ under NIR irradiation, reaching about 99.9% against all types of pathogens at 0.5 mg mL^{-1}, showing its effective and broad-spectrum antibacterial properties. Notably, the experimental group with $InNNi_3$ in the dark also shows moderate antimicrobial activity against *E. coli* and *MRSA*, owing to the electrostatic interactions between the positively charged surface of $InNNi_3$ and the negatively charged bacterial outer membrane. However, this phenomenon is not obvious against *C. albicans*, which might be due to the distinct cell wall structure of fungi that hinders cation penetration.[41–43] Nevertheless, on prolonging the contact time between $InNNi_3$ and *C. albicans* to 2 h, inactivation ability is still observed even without NIR light treatment, decreasing the survival rate of *C. albicans* to approximately 78.7% (Fig. S7†).

Moreover, destroying bacteria within the biofilm is more importantly to promote wound healing since the formation of biofilm can severely prevent drugs from being effectively delivered to wound sites.[44–46] *E. coli* and *MRSA* are prevalent in hospital-acquired infections, leading to challenging chronic infections.[47,48] Therefore, in order to investigate the photothermal killing effect on bacteria within the biofilm, a 3D confocal laser microscope was used to observe the decomposition of biofilm of *E. coli* and *MRSA* by detecting the changes in biofilm thickness stained with Calcein-AM and PI dyes (Fig. 4g and h). Calcein-AM dye with green fluorescence and PI dye with red fluorescence were used to distinguish live and dead bacteria, respectively. In the control groups, regardless of NIR laser exposure, the presence of bright green fluorescence shows the integrity of bacterial biofilms without obvious change. In contrast, the $InNNi_3$ treated group exhibits partial red fluorescence without NIR irradiation, revealing a small quantity of biofilm damage due to electrostatic interactions, similar to the results of colony counting experiments. It should be noted that $InNNi_3$-treated samples under NIR irradiation display intense red fluorescence, with the average intensity exceeding 99% (Fig. S8†), demonstrating significant antibacterial performance of $InNNi_3$ towards biofilm, showing its promising potential as a practical antibiofilm agent.

Electrostatic interaction with microbes and biosafety assessment of $InNNi_3$

The superior antimicrobial and antibiofilm activities of $InNNi_3$ are not only due to its high photothermal conversion efficiency but also its targeted ability. To further reveal the electrostatic interaction between $InNNi_3$ and microbes, the zeta potentials of *E. coli*, *MRSA*, and *C. albicans* before and after the interaction with $InNNi_3$ were measured, as shown in Fig. 5a. $InNNi_3$ possessed a positive zeta potential of 16.70 ± 0.53 mV, ascribed to the unique electronically inverted coordination structure of $InNNi_3$, which results in a positively charged surface with mixed-valence metal cations exposed ($Ni^{\delta+}/In^{\delta+}$). All types of microbes exhibited a negative zeta potential around −20 mV due to the abundance of lipopolysaccharides and alginate on their cell walls.[49–52] The zeta potentials of *E. coli*, *MRSA*, and *C. albicans* treated with $InNNi_3$ showed positive shifts of approximately 7.90 ± 0.58, 10.67 ± 0.34, and 9.90 ± 0.69 mV, respectively, indicating that positively charged $InNNi_3$ are effectively adsorbed on the membrane surface of microbes. To gain deeper insight into the interactions between $InNNi_3$ and microbial cells, the quartz crystal microbalance (QCM) technique was used to monitor the adsorption of bacterial onto the uncoated or $InNNi_3$-coated gold microchips.[53] When microbial suspension was introduced to a QCM chip, the extent of the decrease in the vibration frequency of chip is directly proportional to the amount of microbial adsorption. The QCM adsorption curves for the $InNNi_3$-coated chips exhibited more obvious decline immediately following the injection of microbial suspensions, indicating a rapid microbial adsorption rate. As shown in Fig. 5b, the adsorption of *MRSA*, *E. coli* and *C. albicans* on the $InNNi_3$-coated chip increased to 889.0%, 193.2%, and 420.6%, respectively, as compared with that on the uncoated chip. The significant enhancement of signals demonstrates the strong interaction between $InNNi_3$ and microbes.[54] This rapid rate of microbial adsorption facilitated rapid microbial elimination.

Consequently, the synergistic effect of NIR irradiation combined with the positively charged surface of $InNNi_3$ together contributes to a remarkable 99.9% bacterial inactivation within only 6 min for *MRSA*, *E. coli* and *C. albicans* (Fig. S9†) under light irradiation.

SEM was utilized to reveal the morphological effects of $InNNi_3$ on *E. coli*, *MRSA*, *and C. albicans*. As shown in Fig. 5c–h, the microbes in the control group retained their normal shapes with smooth surfaces regardless of NIR laser irradiation. However, even without NIR treatment, some changes in microbial morphology in the experimental group with $InNNi_3$

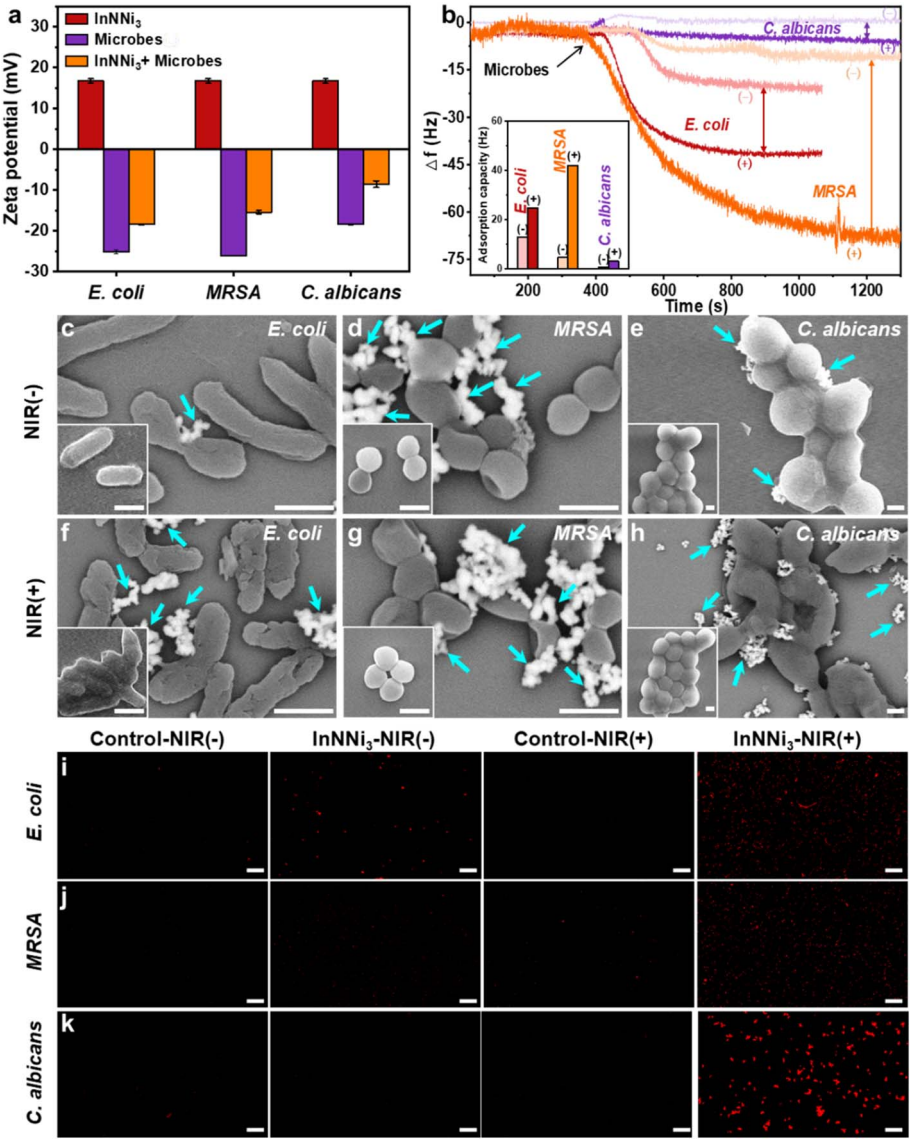

Fig. 5 Characterization of the interaction between $InNNi_3$ and microbes. (a) Zeta potential plots of $InNNi_3$, microbial, and mixed suspensions of $InNNi_3$ and microbes. (b) QCM adsorption profiles of microbes on bare and $InNNi_3$-coated chips (the inset shows the quantitative comparison of QCM adsorption capacity) and (−)/(+) represents uncoated or $InNNi_3$-coated samples, respectively; (c–h) SEM images (insets are their controls without $InNNi_3$ treatment, the arrows represent the $InNNi_3$ photothermal material) and (i–k) live/dead bacterial staining plots of *E. coli*, *MRSA*, and *C. albicans* after treatment with sterile water/$InNNi_3$ for 10 min with or without 808 nm laser irradiation. Scale bar for SEM images, 1 μm; scale bar for fluorescence images, 50 μm.

are observed, showing surface shrinkage. More importantly, the SEM images clearly reveal that $InNNi_3$ nanoparticles are tightly adsorbed onto the microbial surfaces, further demonstrating significant electrostatic interactions between $InNNi_3$ and microbial cells. Experimental groups with both $InNNi_3$ photothermal material and NIR laser exhibit severe structural damage to microbial morphology, including crumple and collapse, which supported the hypothesis that $Ni^{\delta+}/In^{\delta+}$- microbial electrostatic interaction promotes photothermal antibacterial activity. Subsequently, the fluorescence assay for live or dead microbes (Fig. 5i–k) was employed to demonstrate the membrane disruption by the photothermal effect of $InNNi_3$. NuGreen, emitting green fluorescence, penetrates both intact and damaged microbial cells, while EthD-III, which emits red fluorescence, is only taken up by cells with compromised membranes. In the control group and $InNNi_3$-only treated group, microbes mainly emitted green fluorescence, as expected. However, significantly increasing intensity of red fluorescence (Fig. S10†) of dead microbes of *E. coli*, *MRSA*, and *C. albicans* is exhibited in the experimental group with $InNNi_3$ under a NIR laser, indicating an obvious enhancement of the antibacterial effect through the photothermal effect of $InNNi_3$, leading to the complete decomposition of microbial structures. Moreover, durability experiments of cyclic photothermal antibacterial activity against *E. coli*, *MRSA*, and *C. albicans* treated with $InNNi_3$ and NIR laser were also conducted, showing no

decline of performance during 10 cycles (Fig. S11†), which demonstrates the robustness of $InNNi_3$ in photothermal antibacterial applications. Specifically, no obvious changes were detected for the morphology (Fig. S12†), crystalline phase (Fig. S13†), and light absorption properties (Fig. S14†) of $InNNi_3$, even after repetitive antibacterial cycles under NIR light exposure and bacterial contact, further revealing the stability of $InNNi_3$ in photothermal disinfection processes. The results in Table S1† again show the excellent stability of $InNNi_3$ in aqueous solution, with only a very small amount (less than 0.1%) of ions dissolved after 7 days of immersion.

Biological safety of antibacterial agents is essential for their practical applications. The cytotoxicity of $InNNi_3$ was evaluated using the Cell Counting Kit (CCK-8) assay[55] on human embryonic kidney cells (293T) and fibroblasts from mouse embryo (NIH 3T3) cells, revealing survival rates of above 90% at concentrations from 0.25 to 2 mg mL^{-1} (Fig. S15†). Furthermore, from *in vitro* hemolysis testing, which evaluates biomaterial blood compatibility by assessing hemolysis rates, experimental results show that $InNNi_3$-treated erythrocyte solutions had the same color as the negative control (PBS) (Fig. S16a†) and are significantly different from the positive control (0.1% Triton X-100) at concentrations from 0.25 to 2 mg mL^{-1}. According to international standards, a hemolysis rate of more than 5% is considered to be a significant amount of erythrocyte membrane disruption.[56] Thus, in our test, hemolysis rates below the 5% threshold (Fig. S16b†) indicate that $InNNi_3$ has low hemolytic activity and meets the clinical experimental requirement.

Effects of $InNNi_3$ on wound healing acceleration with *MRSA* infection

Due to its excellent photothermal antibacterial activity and low cytotoxicity *in vitro*, the therapeutic effectiveness of $InNNi_3$ has been evaluated on *MRSA*-infected full-thickness skin wounds (diameter = 9 mm) in a rat model. The rats were randomly assigned to four groups: control-NIR (−), $InNNi_3$-NIR (−), control-NIR (+), and $InNNi_3$-NIR(+), representing treatments with or without $InNNi_3$ or NIR laser treatment. Fig. 6a provides a schematic of the wound healing process in rats. The thermal imaging pictures in Fig. 6b show the efficient photothermal conversion of $InNNi_3$ *in vivo* and the local temperature increases up to 13.25 ± 0.45 °C after 10 min under NIR laser irradiation, while the control group only shows an increase of about 2.83 ± 0.66 °C (Fig. 6c). This temperature increase is considered to be pivotal in the healing of *MRSA*-infected wounds. The progress of wound healing under different conditions has been monitored for 14 days with photographs and statistical analysis of the infected skin area. On day 3, the control group exhibited pronounced wound suppuration and biofilm formation, demonstrating the successful establishment of the *MRSA* infection model (Fig. 6d). The $InNNi_3$-NIR(−) group demonstrated markedly decreased suppuration, suggesting that electrostatic interaction between $InNNi_3$ and bacteria also leads to a mild antibacterial effect and subsequent partial wound healing. Notably, the scab formation is found in the $InNNi_3$-NIR(+) group, suggesting a faster rate for wound healing. On day 7, the healing rate of $InNNi_3$–NIR(+) group has impressively reached 55.43 ± 3.96%, and by day 14, the healing rate has the highest value of 93.71 ± 2.63%, compared with rates in the other groups (Fig. 6e and f). To assess the *in vivo* antibacterial efficacy of $InNNi_3$ within infected wounds, wound exudates collected on days 3 and 7 post-wounding were subjected to bacterial plating assays to obtain the resulting colony counts. Fig. 6g and h illustrate that the $InNNi_3$-NIR(+) group achieved a bacterial inhibition rate of about 72% by day 3, and this rate enhanced to nearly 99.9% by day 7, which indicate its stable and continuous antibacterial activity throughout the whole healing process. These findings together demonstrate the potential and reliability of $InNNi_3$ as an antibacterial agent, showing its efficacy in combating infections and ability to accelerate wound healing *via* a photothermal conversion effect and electrostatic targeting.

To comprehensively assess the photothermal effects of $InNNi_3$ on wound tissue regeneration, histological analysis was performed for the detailed understanding of the physiological changes during wound healing. Hematoxylin and eosin (H&E) staining provides insights into the dynamics of inflammatory cells and fibroblasts throughout the wound healing process.[57] In the initial stages, inflammatory cells are essential for clearing wound debris and preventing infection, while unchecked inflammation can impede healing.[58] As shown in Fig. 7a, it is illustrated that by day 3, there are substantial infiltration of inflammatory cells in the control-NIR(−), control-NIR(+) and $InNNi_3$-NIR(−) groups (indicated by red arrows), whereas the $InNNi_3$-NIR(+) group showed a notable decrease in the amount of these cells. By day 10, a continuous decrease of inflammatory cells is further observed in the $InNNi_3$-NIR(+) group (red arrows), indicating that the photothermal therapy of $InNNi_3$ with NIR irradiation effectively mitigated inflammation, fostering a suitable environment for tissue repairing. Fibroblasts are beneficial for the proliferative stage of wound healing. As depicted in Fig. 7a, the $InNNi_3$-NIR(+) group exhibited enhanced fibroblast migration (blue arrows) on day 10. These cells migrate to the wound site and generate extracellular matrix components, such as collagen, which is vital for the formation of granulation tissue.[59] The granulation tissue serves not only to bridge the wound gap but also to provide a scaffold for epithelial cell migration.[60] The $InNNi_3$-NIR(+) group shows a thicker granulation tissue, with a higher average thickness of 1.17 ± 0.01 mm, compared to that of control-NIR(−), control-NIR(+) and $InNNi_3$-NIR(−) groups, which have average thicknesses of 0.836 ± 0.02 mm, 0.824 ± 0.03 mm, and 0.892 ± 0.01 mm, respectively, as shown in Fig. 7d. The interaction between fibroblasts and growth factors facilitates wound contraction and maturation, as well, promoting the formation of scar finally.[61] The $InNNi_3$-NIR(+) group exhibited the narrowest average scar width, at approximately 2.58 ± 0.05 mm, in contrast to that of control-NIR(−), control-NIR(+) and $InNNi_3$-NIR(−) groups, in which 4.88 4.52 ± 0.17 mm and 4.08 ± 0.03 mm were measured, respectively (Fig. 7e). These results indicated that $InNNi_3$ enhances organized deposition of collagen and suppresses aberrant and random accumulation of collagen,

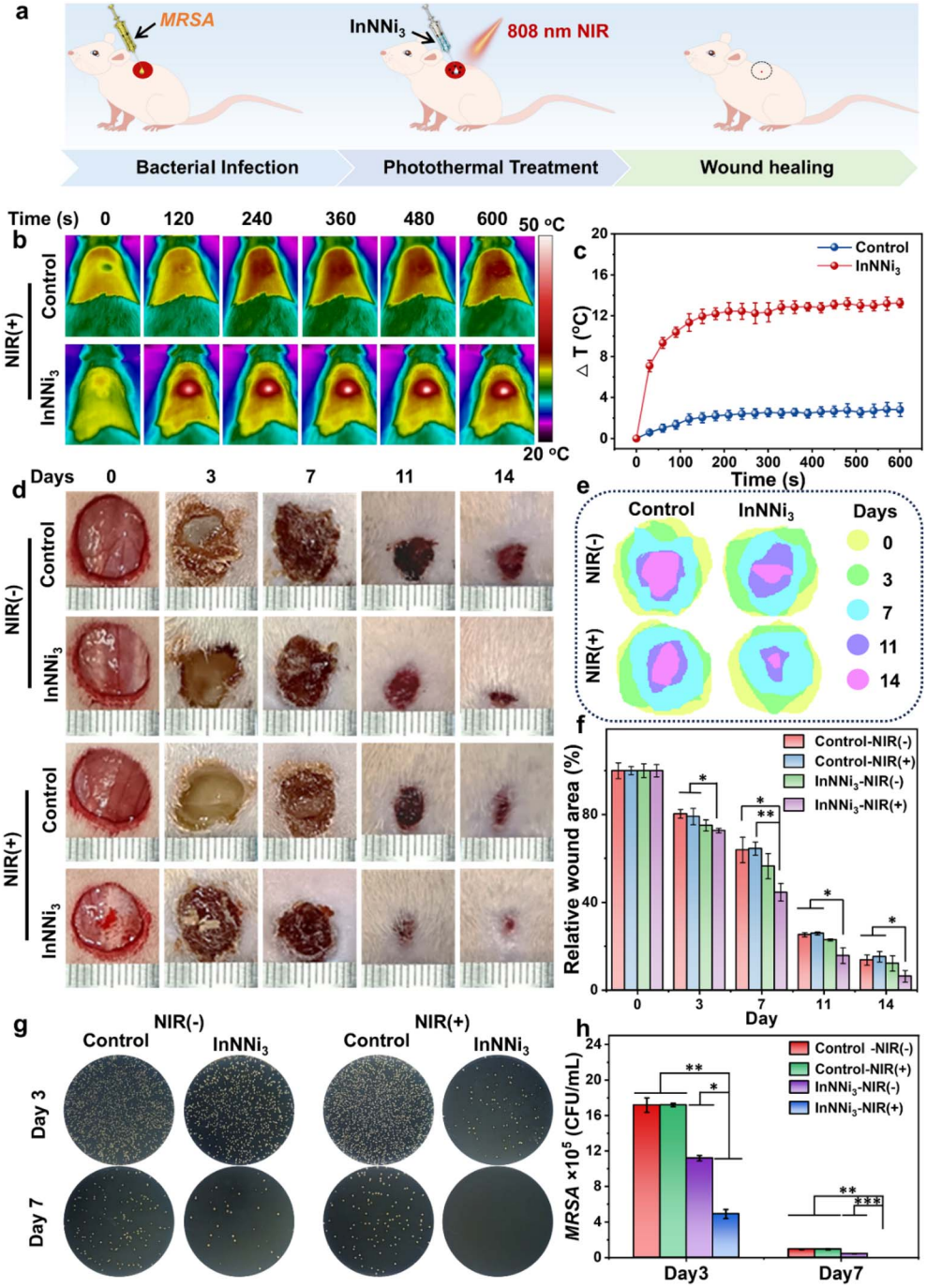

Fig. 6 Evaluation of the properties of accelerated wound healing. (a) Schematic diagram of the wound healing promotion experiment. (b) Thermograms of SD rats and (c) photothermal heating curves of the wound site treated with sterile water and $InNNi_3$ (0.5 mg mL^{-1}) irradiated with a 808 nm NIR laser at 1 W cm^{-2} for 10 min (body temperature of control rats was 36.9 °C, $n = 3$). (d) Representative photographs of rat skin wounds on days 0, 3, 7, 11 and 14. (e) Schematic images showing the wound healing process of different treatment groups from day 0 to 14. (f) Quantitative plot of wound area as a function of time since treatment ($n = 3$). (g) Pictures of colony growth of *MRSA* on LB agar plates and (h) the number of bacteria at the wound site on day 3 and day 7. *MRSA* was derived from the wound area on day 3 and day 7. Data are expressed as mean ± SD, $n = 3$. * indicates statistically significant differences (*$p < 0.05$, **$p < 0.01$, and ***$p < 0.001$).

which may contribute to the formation of more mature scars with narrower widths.[62,63]

Besides, quantitative analysis *via* Masson trichrome staining reveals significant differences in collagen deposition among the various groups (Fig. 7b), with the $InNNi_3$-NIR(+) group exhibiting the highest rate at 60.52 ± 5.54% (Fig. 7f). This rate outperforms those of the control-NIR(−), control-NIR(+) and $InNNi_3$-NIR(−) groups, calculated as 21.68 ± 1.05%, 21.19 ± 0.18% and 32.54 ± 2.33%, respectively. These findings again suggest that $InNNi_3$ significantly stimulates collagen production. Angiogenesis is

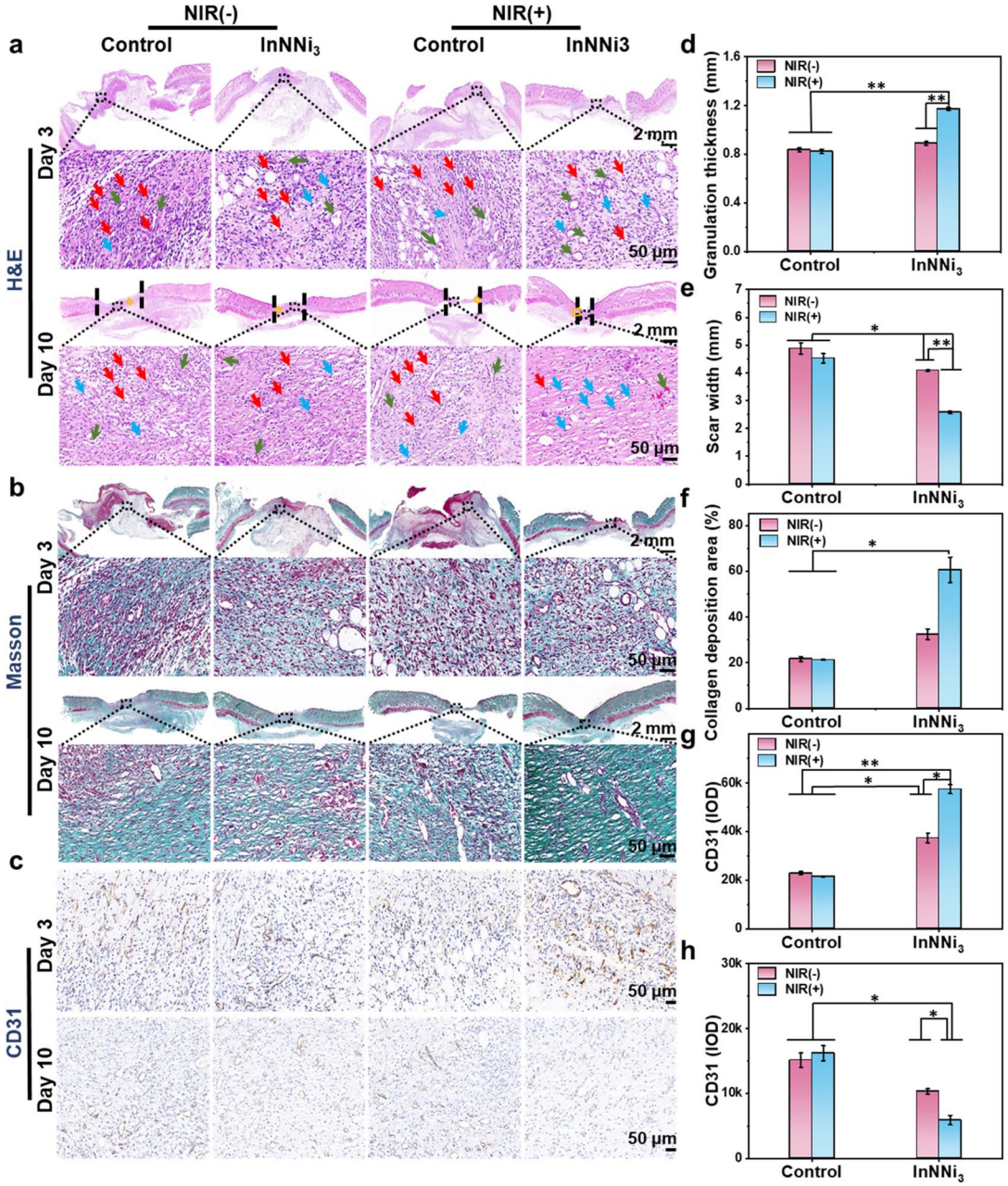

Fig. 7 Histologic study of skin after different treatments. (a) H&E staining and (b) Masson staining on days 3 and 10 (red arrows: inflammatory infiltrating cells, blue arrows: fibroblasts; green arrows: neovascularization; orange double arrows: granulation tissue; black dashed spacing: scar width). (c) Immunohistochemical staining of newly formed blood CD31 in the wound area on days 3 and 10. Quantitative analysis of day 10 (d) regenerating granulation tissue and (e) wound scar width from (a). (f) Quantitative analysis of day 10 collagen deposition from (b). Quantitative analysis of microvessels on (g) day 3 and (h) day 10 from (c). Data are expressed as mean ± SD, $n = 3$. * indicates statistically significant differences (*$p < 0.05$; **$p < 0.01$).

a critical determinant in the wound healing process, suppling oxygen and nutrients for the wound bed.[64] Our quantitative analysis of angiogenesis using CD31 immunohistochemical staining (Fig. 7c), expressed as the integral optical density (IOD), demonstrates a significantly enhanced value in the InNNi$_3$-NIR(+) group on day 3, with an IOD of 57 471 ± 1764, which is much higher than those of control-NIR(−), control-NIR(+) and InNNi$_3$-NIR(−) groups, in which IODs were measured as 22 829 ± 705, 21 547 ± 119, and 37 398 ± 1959, respectively (Fig. 7g). By day 10, however, a notable reduction in angiogenic activity was observed in the InNNi$_3$-NIR(+) group. This reduction might be associated with the intrinsic regulatory mechanisms that suppress angiogenesis once the wound has reached an adequate level of vascularization, thereby preventing unwarranted angiogenesis (Fig. 7h).[65] This photothermal antibacterial strategy reduces inflammation, stimulates granulation tissue formation, and promotes collagen deposition and early-stage angiogenesis, significantly accelerating the wound healing process.

The *in vivo* biocompatibility of $InNNi_3$ was examined *via* histological evaluation of vital organs, including the heart, liver, spleen, lungs, and kidneys, in rats under different treatments (Fig. S17†). Hematoxylin and eosin (H&E) staining results revealed that, during the testing period, the organ tissues on day 3 and day 10 across all experimental groups exhibited no signs of abnormality or pathological alterations, thereby demonstrating the *in vivo* safety of $InNNi_3$. Furthermore, to track the general health status of the rats, their body weights throughout the 14 day treatment period were monitored. As shown in Fig. S18,† no matter whether the rats were from the experimental or control groups, the body weights of rats in each group increased smoothly, without any irregular weight fluctuations. This consistent weight further exhibits the safety of the photothermal treatment strategy with $InNNi_3$, suggesting that $InNNi_3$ has excellent biocompatibility with various organs, which shows its practical application for clinical antibacterial therapy and wound healing without impacting the health of organisms.

Conclusions

In summary, a novel photothermal antibacterial nanoplatform based on $InNNi_3$ antiperovskite has been successfully constructed. Under NIR laser irradiation, *MRSA*, *E. coli*, *C. albicans* and their biofilms can be effectively eliminated *via* the high light-to-heat conversion efficiency of $InNNi_3$, which is contributed by the quasi-continuous energy levels for full-spectrum absorption. The electronically inverted coordination of $InNNi_3$ endows it with a positively charged surface for the strong electrostatic interaction with microbes, which further enhances the antibacterial activity. High photothermal stability and cyclic antibacterial activity of $InNNi_3$ were also achieved. Both *in vitro* and *in vivo* experiments demonstrate the low cytotoxicity and excellent biocompatibility of $InNNi_3$. Benefiting from the near-unity photothermal-induced antibacterial ability, the healing rate for infection wound is significantly improved, *via* the promoting effect of reducing inflammation, stimulating collagen deposition, enhancing the early expression of CD31, and fostering the regeneration of the dermis and skin appendages. This work not only reports a new class of efficient photothermal materials but also presents a safe and effective solution for solving the severe problem of drug resistance of pathogens and a promising strategy for treating open wound infections.

Ethical statement

Animal experiments were performed in accordance with the Guidelines for the Care and Use of Laboratory Animals of the National Research Council and approved by the Ethics Committee for Laboratory Animals of Fujian Medical University (No: IACUC FJMU 2023 - Y-0552).

Data availability

All relevant data have been included in the main text and the ESI.†

Author contributions

X. J. W. conceived the project design, analyzed the experimental data and wrote the paper. L. B. H. synthesized the photothermal material, performed characterization studies, *in vitro* antibacterial experiments, photothermal performance experiments, biocompatibility experiments, and wound healing experiments. Q. Y. C., Z. S., Y. Y. and Z. J. H. performed wound healing experiments. Z. Y. C., Y. H. L., H. S., Z. G. Z. and J. Y. performed theoretical calculations, provided methods for the synthesis of materials. H. Z. and H. L. H. revised the paper.

Conflicts of interest

There are no conflicts to declare.

Acknowledgements

This work was financially supported by the Natural Science Foundation of China (grant numbers 22102029, U1805234, 22109024, and 22479028), Natural Science Foundation of Fujian Province of China (grant numbers 2019J01264, 2023H6011 and 2021J01595), Fu-Xia-Quan National Independent Innovation Demonstration Zone Collaborative Innovation Platform Project (2022FX3), Major Scientific Research Program for Young and Middle-aged Health Professionals of Fujian Province, China (2023ZQNZD020), Program for Innovative Research Team in Science and Technology in Fujian Province University, 100 Talents Program of Fujian Province, Fujian-Taiwan Science and Technology Cooperation Base of Biomedical Materials and Tissue Engineering (2021D039), and Scientific Research Start-up Fund for High-Level Talents in Fujian Normal University.

Notes and references

1 S. Guo and L. A. DiPietro, *J. Dent. Res.*, 2010, **89**, 219–229.
2 A. Uberoi, A. McCready-Vangi and E. A. Grice, *Nat. Rev. Microbiol.*, 2024, **22**, 507–521.
3 R. Luo, Y. Liang, J. Yang, H. Feng, Y. Chen, X. Jiang, Z. Zhang, J. Liu, Y. Bai, J. Xue, S. Chao, Y. Xi, X. Liu, E. Wang, D. Luo, Z. Li and J. Zhang, *Adv. Mater.*, 2023, **35**, 2208395.
4 A. Cioce, A. Cavani, C. Cattani and F. Scopelliti, *Cells*, 2024, 13.
5 C. Cheung, V. Biousse, P. Keane, E. Schiffrin and T. Wong, *Nat. Rev. Dis. Primers*, 2022, **8**, 15.
6 D. G. Armstrong, J. R. Ingelfinger, A. J. M. Boulton and S. A. Bus, *N. Engl. J. Med.*, 2017, **376**, 2367–2375.
7 Y. Zheng, J. Wu, Y. Zhu and C. Wu, *Chem. Sci.*, 2023, **14**, 29–53.
8 R. Mirzaei, M. Yunesian, S. Nasseri, M. Gholami, E. Jalilzadeh, S. Shoeibi and A. Mesdaghinia, *Sci. Total Environ.*, 2018, **619–620**, 446–459.
9 X. Zhu, A. F. Radovic-Moreno, J. Wu, R. Langer and J. Shi, *Nano Today*, 2014, **9**, 478–498.
10 C. Karthikeyan, K. Varaprasad, A. Akbari-Fakhrabadi, A. S. H. Hameed and R. Sadiku, *Carbohydr. Polym.*, 2020, **249**, 116825.

11 J.-J. Li, Y. Hu, B. Hu, W. Wang, H. Xu, X.-Y. Hu, F. Ding, H.-B. Li, K.-R. Wang, X. Zhang and D.-S. Guo, *Nat. Commun.*, 2022, **13**, 6279.
12 S. Mei, X. Xu, R. D. Priestley and Y. Lu, *Chem. Sci.*, 2020, **11**, 12269–12281.
13 J. Zhou, W. Wang, Q. Zhang, Z. Zhang, J. Guo and F. Yan, *Chem. Sci.*, 2022, **13**, 6967–6981.
14 C. Aloke and I. Achilonu, *Microb. Pathog.*, 2023, **175**, 105963.
15 B. Aslam, W. Wang, M. I. Arshad, M. Khurshid, S. Muzammil, M. H. Rasool, M. A. Nisar, R. F. Alvi, M. A. Aslam, M. U. Qamar, M. K. F. Salamat and Z. Baloch, *Infect. Drug Resist.*, 2018, **11**, 1645–1658.
16 C. Mao, Y. Xiang, X. Liu, Z. Cui, X. Yang, Z. Li, S. Zhu, Y. Zheng, K. W. K. Yeung and S. Wu, *ACS Nano*, 2018, **12**, 1747–1759.
17 X. Qi, Y. Xiang, E. Cai, X. Ge, X. Chen, W. Zhang, Z. Li and J. Shen, *Coord. Chem. Rev.*, 2023, **496**, 215426.
18 S. Hao, H. Han, Z. Yang, M. Chen, Y. Jiang, G. Lu, L. Dong, H. Wen, H. Li, J. Liu, L. Wu, Z. Wang and F. Wang, *Nano-Micro Lett.*, 2022, **14**, 178.
19 X. Li, J. F. Lovell, J. Yoon and X. Chen, *Nat. Rev. Clin. Oncol.*, 2020, **17**, 657–674.
20 M. Kim, J. H. Lee and J. M. Nam, *Adv. Sci.*, 2019, **6**, 1900471.
21 Z. Miao, S. Chen, C.-Y. Xu, Y. Ma, H. Qian, Y. Xu, H. Chen, X. Wang, G. He, Y. Lu, Q. Zhao and Z. Zha, *Chem. Sci.*, 2019, **10**, 5435–5443.
22 X. Huang, W. Zhang, G. Guan, G. Song, R. Zou and J. Hu, *Acc. Chem. Res.*, 2017, **50**, 2529–2538.
23 D. Xu, Z. Li, L. Li and J. Wang, *Adv. Funct. Mater.*, 2020, **30**, 2000712.
24 G. Chakraborty, I.-H. Park, R. Medishetty and J. J. Vittal, *Chem. Rev.*, 2021, **121**, 3751–3891.
25 Z. Mi, P. Yang, R. Wang, J. Unruangsri, W. Yang, C. Wang and J. Guo, *J. Am. Chem. Soc.*, 2019, **141**, 14433–14442.
26 G. Li, Q. Yue, P. Fu, K. Wang, Y. Zhou and J. Wang, *Adv. Funct. Mater.*, 2023, **33**, 2213810.
27 Z. Lv, S. He, Y. Wang and X. Zhu, *Adv. Funct. Mater.*, 2021, **10**, 2001806.
28 J. Han, Q. Liu, Y. Yang and H. B. Wu, *Chem. Sci.*, 2025, **16**, 3788–3809.
29 X. Meng, L. Liu, S. Ouyang, H. Xu, D. Wang, N. Zhao and J. Ye, *Adv. Mater.*, 2016, **28**, 6781–6803.
30 Y. Chen, Z. Fan, Z. Zhang, W. Niu, C. Li, N. Yang, B. Chen and H. Zhang, *Chem. Rev.*, 2018, **118**, 6409–6455.
31 H. S. Jung, P. Verwilst, A. Sharma, J. Shin, J. L. Sessler and J. S. Kim, *Chem. Soc. Rev.*, 2018, **47**, 2280–2297.
32 Y. Wang, H. Zhang, J. Zhu, X. Lü, S. Li, R. Zou and Y. Zhao, *Adv. Mater.*, 2019, **32**, 1905007.
33 Z. Gong, X. Xiang, W. Zhong, C. Jia, P. Chen, N. Zhang, S. Zhao, W. Liu, Y. Chen and Z. Lin, *Angew. Chem., Int. Ed.*, 2023, **62**, e202308775.
34 S. V. Krivovichev, *Coord. Chem. Rev.*, 2024, **498**, 215484.
35 R. S. Ningthoujam and N. S. Gajbhiye, *Prog. Mater. Sci.*, 2015, **70**, 50–154.
36 R. A. Karaballi, Y. Esfahani Monfared and M. Dasog, *Langmuir*, 2020, **36**, 5058–5064.
37 Y. Wu, P. Liu, B. Mehrjou and P. K. Chu, *Adv. Mater.*, 2023, **36**, 2305940.
38 Z. Deng, D. Ni, D. Chen, Y. Bian, S. Li, Z. Wang and Y. Zhao, *InfoMat*, 2021, **4**, e12252.
39 J. Zhang, Y. Tu, L. Zhang, S. He, C. Zhong, J. Ke, L. Wang, C. Cui, H. Song, L. Du and Z. Cui, *ACS Nano*, 2024, **18**, 32077–32087.
40 H. Zhang, W. Xia, H. Shen, W. Guo, Z. Liang, K. Zhang, Y. Wu, B. Zhu and R. Zou, *Angew. Chem.*, 2019, **132**, 1887–1893.
41 N. A. R. Gow and B. Hube, *Curr. Opin. Microbiol.*, 2012, **15**, 406–412.
42 C. Ibe and C. A. Munro, *J. Fungi*, 2021, **7**, 739.
43 J. P. Martínez, M. L. Gil, J. L. López-Ribot and W. L. Chaffin, *Clin. Microbiol. Rev.*, 1998, **11**, 121–141.
44 J. Wu, W. Wang, J. Shen, N. Zhou, Y. Li, B. Z. Tang and M. Zhang, *Adv. Funct. Mater.*, 2024, **34**, 2312374.
45 M. Qin, X. Zhang, H. Ding, Y. Chen, W. He, Y. Wei, W. Chen, Y. K. Chan, Y. Shi, D. Huang and Y. Deng, *Adv. Mater.*, 2024, **36**, 2402530.
46 A. Dey, M. Yadav, D. Kumar, A. K. Dey, S. Samal, S. Tanwar, D. Sarkar, S. K. Pramanik, S. Chaudhuri and A. Das, *Chem. Sci.*, 2022, **13**, 10103–10118.
47 N. A. Turner, B. K. Sharma-Kuinkel, S. A. Maskarinec, E. M. Eichenberger, P. P. Shah, M. Carugati, T. L. Holland and V. G. Fowler, *Nat. Rev. Microbiol.*, 2019, **17**, 203–218.
48 B. W. Trautner and R. O. Darouiche, *Am. J. Infect. Control*, 2004, **32**, 177–183.
49 L. Pasquina-Lemonche, J. Burns, R. D. Turner, S. Kumar, R. Tank, N. Mullin, J. S. Wilson, B. Chakrabarti, P. A. Bullough, S. J. Foster and J. K. Hobbs, *Nature*, 2020, **582**, 294–297.
50 R. Sadamoto, K. Niikura, P. S. Sears, H. Liu, C.-H. Wong, A. Suksomcheep, F. Tomita, K. Monde and S.-I. Nishimura, *J. Am. Chem. Soc.*, 2002, **124**, 9018–9019.
51 R. Fischl, K. Bertelsen, F. Gaillard, S. Coelho, G. Michel, M. Klinger, C. Boyen, M. Czjzek and C. Hervé, *Glycobiology*, 2016, **26**, 973–983.
52 X. Wang, Y. Liu, T. Wu, B. Gu, H. Sun, H. He, H. Gong and H. Zhu, *Bioorg. Chem.*, 2023, **134**, 106448.
53 Y. Shen, H. Lin, M. Yang, X. Gong, B. Guan, Y. Han, S. Wang and Y. Wang, *Adv. Mater.*, 2023, **35**, 2210936.
54 Y. Shen, S. Li, R. Qi, C. Wu, M. Yang, J. Wang, Z. Cai, K. Liu, J. Yue, B. Guan, Y. Han, S. Wang and Y. Wang, *Angew. Chem., Int. Ed.*, 2021, **61**, e202110938.
55 J. Chen, Y. Yu, H. Li, Q. Hu, X. Chen, Y. He, C. Xue, F. Ren, Z. Ren, J. Li, L. Liu, Z. Duan, G. Cui and R. Sun, *Mol. Cancer*, 2019, **18**, 33.
56 X. Zhao, Y. Chen, R. Niu, Y. Tang, Y. Chen, H. Su, Z. Yang, X. Jing, H. Guan, R. Gao and L. Meng, *Adv. Mater.*, 2023, **36**, 2307839.
57 L. Wang, Q. Su, Y. Liu, T. Yimamumaimaiti, D. Hu, J.-J. Zhu and J.-R. Zhang, *Chem. Sci.*, 2022, **13**, 12136–12143.
58 W. Wang, P. Gao, H. Gui, X. Wei, H. Zhang and X. Wang, *Coord. Chem. Rev.*, 2025, **522**, 216205.
59 T. Faial, *Nat. Genet.*, 2015, **47**, 568.

60 M. Li, Y. Liang, Y. Liang, G. Pan and B. Guo, *Chem. Eng. J.*, 2022, **427**, 132039.
61 P. Mostafalu, G. Kiaee, G. Giatsidis, A. Khalilpour, M. Nabavinia, M. R. Dokmeci, S. Sonkusale, D. P. Orgill, A. Tamayol and A. Khademhosseini, *Adv. Funct. Mater.*, 2017, **27**, 1702399.
62 Y. Wang, Y. Zhang, T. Li, K. Shen, K. J. Wang, C. Tian and D. Hu, *Adv. Mater.*, 2023, **35**, 2303642.
63 R. Sklenářová, N. Akla, M. J. Latorre, J. Ulrichová, J. Franková and J. Funct, *Biomater*, 2022, **13**, 249.
64 A. P. Veith, K. Henderson, A. Spencer, A. D. Sligar and A. B. Baker, *Adv. Drug Delivery Rev.*, 2019, **146**, 97–125.
65 K. Zha, W. Zhang, W. Hu, M. Tan, S. Zhang, Y. Yu, S. Gou, P. Bu, B. Zhou, Y. Zou, Y. Xiong, B. Mi, G. Liu, Q. Feng and K. Cai, *Adv. Funct. Mater.*, 2023, **34**, 2308145.